

Harnessing Strong Gravitational Lensing to Constrain Mass and Light in Galaxy Clusters

SIMON D. MORK¹ AND MICHAEL D. GLADDERS^{1,2}

¹*Department of Astronomy and Astrophysics, University of Chicago, 5640 South Ellis Avenue, Chicago, IL 60637, USA*

²*Kavli Institute for Cosmological Physics, University of Chicago, 5640 South Ellis Avenue, Chicago, IL 60637, USA*

ABSTRACT

We present a comprehensive analysis of the mass and light distributions in cluster-scale strong gravitational lens systems. Strong gravitational lensing is a rare phenomenon in the universe in which massive foreground galaxies magnify and multiply-image background source galaxies into magnificent arcs. The COOL-LAMPS collaboration (Chicago Optically-Selected Lenses Located at the Margins of Public Surveys) has discovered and confirmed hundreds lensing systems via color-magnitude selection and visual inspection with lens redshifts ranging from ~ 0.2 to ~ 1.2 in DECaLS (Dark Energy Camera Legacy Survey) Data Release 8 images, of which 179 are analyzed here. In this work, we compute parametric estimates of the Einstein-radius-enclosed mass and luminosity for each system using only two measured parameters: the Einstein radius and the photometric galaxy-cluster redshift. We find that the total-mass-to-light ratio has little correlation with the redshift of the cluster, and we also parameterize the stellar-to-total-mass ratio as a function of physical distance in kiloparsecs from the center of the BCG. This work will lay out a blueprint for studying larger samples of cluster-scale strong gravitational lens candidates in upcoming imaging surveys such as Rubin/LSST (Legacy Survey of Space and Time), in which an algorithmic treatment of lensing systems will be needed due to the sheer volume of data these surveys will produce.

1. INTRODUCTION

Measuring mass in galaxy clusters can be done in a variety of ways. Considering galaxies as an aggregate of stars, stellar structure theory places strong constraints on the observed luminosity of a star as a function of its mass (Kuiper 1938; Wang & Zhong 2018). For a galaxy with a uniform stellar population in which its light functionally traces its mass, one can simply integrate over a given aperture and convert the observed flux to a luminosity and on to a stellar mass measurement (Presotto et al. 2014). Galaxies and galaxy clusters are objects that are made of far more than just stars though (Zwicky 1933; Rubin 1986). Hot intracluster gas contributes significantly to the total mass in galaxy clusters, and this gas radiates strongly in the x-ray as a function of its temperature (e.g., Kellogg et al. 1972; Forman et al. 1972). X-ray observatories, like the Chandra X-ray Observatory, are able to make direct observations of this x-ray emission and thus infer the mass of the gas in addition to previous methods of characterizing stellar mass (e.g.,

Markevitch & Vikhlinin 2007). More than just gas and stars, galaxies and galaxy clusters are complex objects that also incorporate dark matter halos in their overall structure at a typical factor many times greater than the amount of baryonic matter contained in any single galaxy (Navarro et al. 1996; Hradecky et al. 2000). However, since astronomers and physicists have yet to link the presence of dark matter to any physical observable, quantifying the amount of dark matter in a given system is only indirectly possible. Galaxy clusters are generally virialized systems, and one can obtain a mass estimate for a given galaxy or galaxy cluster by simply measuring the velocity dispersion of cluster galaxies along the line of sight in addition to the virial radius of the individual cluster (Bryan & Norman 1998). However, this measurement assumes a state of dynamical equilibrium for each cluster, which may not apply in the case of recent mergers (e.g., Lourenço et al. 2020), for example. All three of these measurements are beneficial in their own way, but each relies on some underlying assumption regarding the state of the system at hand in order to measure mass. This is where we turn to gravitational lensing for help.

Gravitational lensing is a phenomena where mass in the universe causes the path of light rays which pass

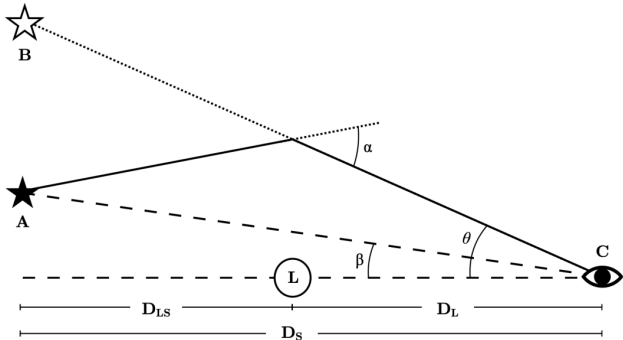


Figure 1. A descriptive visualization of the simplest case of gravitational lensing adapted from Levine (2022) with an object at position A being lensed by lens L causing the observer at position C to view it at position B. Note the angle θ as the Einstein radius which characterizes the angular separation between the lensed image at position B and the line-of-sight from the observer to lens L.

near said mass to bend as a result of general relativity (Einstein 1936). The visualization of lensing in Figure 1 obeys Equations (1) and (2).

$$\vec{\beta} = \vec{\theta} - \vec{\alpha}(\vec{\theta}) \quad (1)$$

$$\vec{\alpha}(\vec{\theta}) = \frac{D_{LS}(z_L, z_S)}{D_S(z_S)} \vec{\hat{\alpha}}(\vec{\theta}) \quad (2)$$

While, technically, all mass in the universe causes some degree of gravitational lensing and obeys Equations (1) and (2), only objects in the universe with the highest projected surface mass density, such as galaxies and galaxy clusters, are capable of producing multiple images of background sources (Shajib et al. 2022). The visible effect of lensing by galaxies and galaxy clusters, henceforth referred to as “strong” lensing, creates highly distorted, magnified, and multiply-imaged images of galaxies that are located behind the lens relative to the observer typically in an arclike shape (e.g., Gunn et al. 1979; Rivera-Thorsen et al. 2017; Napier et al. 2023). Galaxy clusters produce the strongest lensing effect and are the best “natural telescopes” in the universe (Lotz et al. 2017). This allows us to peer into the high-redshift universe at angular resolutions that would be impossible to achieve with any observational facility currently available. As derived in Remolina González et al. (2020), the mass of many different individual gravitational lens systems are able to be algorithmically constrained knowing the angle θ between the brightest cluster galaxy (BCG) and lensed source arc, which is the Einstein radius described in Figure 1, the redshift of the lens (lensing galaxy), and the redshift of the source (lensed background galaxy). This allows one to quickly estimate the core mass interior to the Einstein radius of

a galaxy cluster with minimal scatter on order of $\approx 10\%$ using Equations (3) and (4).

$$\Sigma_{\text{cr}}(z_L, z_S) = \frac{c^2}{4\pi G} \times \frac{D_S(z_S)}{D_L(z_L)D_{LS}(z_L, z_S)} \quad (3)$$

$$M(< \theta_E) = \Sigma_{\text{cr}}(z_L, z_S) \times \pi(D_L(z_L)\theta_E)^2 \quad (4)$$

Since Equations (3) and (4) are agnostic of the distribution of mass within the Einstein radius itself, it offers a simple, efficient, and powerful tool to measure mass at high density scales provided the lensing geometry is simple enough to be described by a single, roughly circular projected mass distribution. This method allows one to measure the mass of galaxies at a higher density scale and correspondingly smaller radii than typical mass measurements of M_{200} or M_{500} . Here, 200 and 500 refer to the radius from the BCG at which the mean density of the cluster is 200 or 500 times the mean density of the universe respectively (White 2001).

While mass is an important metric to consider even by itself, the scientific value of this measurement can be amplified greatly by measuring luminosity from an observed flux in addition to mass. Constraining light allows us to directly measure the total-mass-to-light ratio of galaxy clusters in addition to measuring the stellar-to-total-mass ratio. Both of these parameters are important for testing cosmological simulations, as the evolution of how these parameters behave over a wide range of distance scales and redshifts is informed by underlying cosmological parameters that created the simulation in the first place.

Throughout this paper, we adopt a flat Λ CDM cosmology with $\Omega_m = 0.3$, $\Omega_\Lambda = 0.7$, and $H_0 = 70$ km/s/Mpc. All photometric calculations were done using the AB magnitude system using the *grz* filters on the Dark Energy Camera (DECam, Honscheid & DePoy 2008).

2. MEASUREMENT

We begin by collating a sample of galaxy clusters and groups that exhibit visual evidence of strong gravitational lensing. Leveraging a large number of investigators with a wide variety of experience levels, the COOL-LAMPS collaboration has found hundreds of new strong-lensing galaxy clusters located in public imaging surveys primarily through direct visual inspection of Legacy Survey Data Release 8 DECaLS (Dey et al. 2019) images. Since the measurement described in Remolina González et al. (2020) works best when the tangentially lensed arcs trace out some portion of an ring with radius equal to the Einstein radius centered on the BCG, the most suitable clusters for this analysis are ones where the most obvious lensed arc is a roughly circular arc with

projected center located at or very near to the BCG. 179 strong-lensing systems were selected from COOL-LAMPS data archives based on this ranking, since any systems with complex morphology are less likely to be well described by this simple model. A collage to visualize the kinds of clusters and lenses considered in this work is shown in Figure 2.

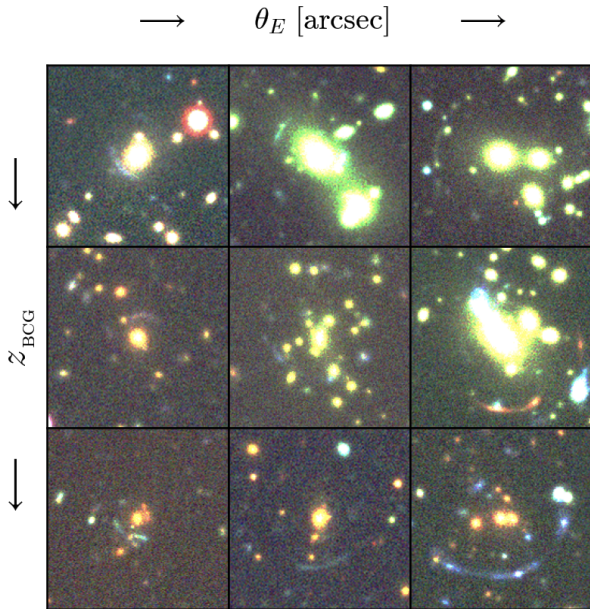


Figure 2. A sample of 9 strong gravitational lenses used in this work. Note the presence of a visually-obvious tangentially-lensed source-galaxy arc in all of the images.

With our sample in hand, we then constrained the three fundamental parameters needed to generate a mass estimate: Einstein radius, lens redshift, and source redshift.

2.1. Einstein Radius

Of the three parameters necessary to generate an enclosed mass for any given cluster, the Einstein radius is easily the most important. Drawing on the methodology of Remolina González et al. (2020), we define the Einstein radius for each system as the radius of a circle centered on each cluster’s BCG which minimizes the total residual distance between the perimeter of the circle and each of the three most readily identifiable bright “clumps” in the lensed arcs for each lensing system. Square image cutouts centered on the coordinates of the BCG were initially queried from the Legacy Survey DR9 DECaLS server, and each one was then loaded into an SAOImageDS9 RGB frame where the z -band corresponded to the red channel, the r -band corresponded to the green channel, and the g -band corresponded to the

blue channel. All three channels were then automatically scaled to the DS9 “zscale” setting, as this scaling made visual identification of lensed image families the easiest by eye. Contours were applied to the image based on its g -band flux, since this band strikes a good balance between making both the BCG and lensed arcs visible, in order to identify the point of peak surface brightness for the BCG and similar peaks in surface brightness in the clumps of each tangentially lensed arc. The coordinates of these four points (the BCG center and three points along each arc) were identified and saved using the command-line DS9 “iexam” function. In order to place error bars on the Einstein radius, the three positional constraints for each circular arc were bootstrapped 1000 times and pushed through the minimization algorithm. The mean and standard deviation for the resulting 1000 values were adopted as the value and error for Einstein radius respectively.

2.2. Lens (BCG) Redshift

Constraining the lens redshift is important to scale the measured Einstein radius to a cosmologically sensible angular diameter distance (Remolina González et al. 2020). Since cluster-member galaxies in the lens are predominantly “elliptical”, “red-sequence”, or “early-type” galaxies, they fall on a predictable trend as a function of redshift in color-magnitude space (Gladders & Yee 2000). We adopt the codebase implemented in Levine (2022) to measure the characteristic redshift of each lensing system. The algorithm takes in a list of RA and Dec coordinates of the BCG as identified in the Einstein radius step, identifies cluster member galaxies along the line-of-sight within a radius defined by the user (one arcminute in our case) as informed by this color-magnitude relation, and returns a list of photometric redshifts transformed from colors of each cluster member identified in the search radius. This generated a list of photometric redshifts for all of the identified cluster members in a one arcminute aperture. The observed cluster-member galaxy distribution consists of cluster members (both galaxies on the red sequence, and intrinsically bluer galaxies) and galaxies along the line of sight which occupy a broad range of colors both bluer and redder than the cluster red-sequence. Because the bluer cluster members creates a lopsided color distribution, which can bias the estimated cluster redshift low, and the measured scatter high, we focus only on apparent red-sequence members to estimate the color (and thus redshift) uncertainty for a given system.

For the richest clusters in our sample in which individual cluster measurements of the measured width of the cluster red sequence are robust, we noted that this

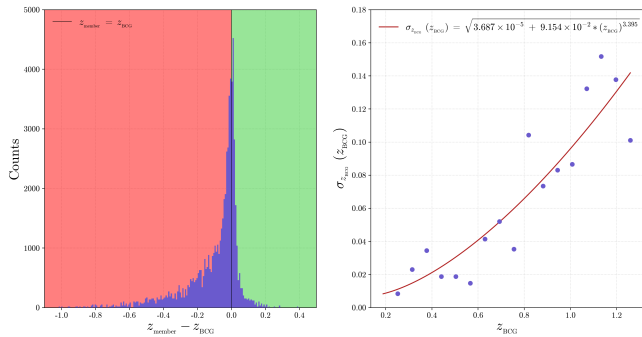


Figure 3. On the left, a histogram of the photometric BCG-normalized redshifts for all tagged non-BCG cluster-member galaxies in this work. The red region of the histogram with the larger scatter is excluded from further calculations due to possible non-cluster-member interlopers. The green region is representative of bona-fide cluster members. On the right, we take the green region of the plot and separate it into 17 photometric redshift bins based on range of our sample. The scatter in each of those bins is plotted with a best-fit functional description overlotted in red.

uncertainty increased as a function of redshift. This is to be expected, even in the absence of a true increase in scatter in the rest frame, due to increasing photometric uncertainties for fainter galaxies. In addition, within the fixed wavelength range of our rest-frame observational bandpasses, we observe a bluer portion of the spectrum from any given galaxy as the effects of cosmological redshifting pushes the galaxy’s rest-frame spectrum redward. The measured photometric redshift from this bluer light is more sensitive to minor differences between the star formation history and stellar properties between individual galaxies, resulting in increased scatter for our predicted redshifts. In order to account for this increasing uncertainty as a function of redshift, we sorted all of the clusters based on their BCG photometric redshift into 17 redshift bins equally spaced between the minimum and maximum value of the BCG photometric redshift for the entire sample of 179 clusters. This strikes a good balance between redshift granularity and total cluster members identified in each bin for different systems. We compute the color scatter (and hence redshift scatter) from all identified cluster-member galaxies within each redshift bin. We then fit a function of the form $f(z) = \sqrt{a + bz^c}$ to the data in order to parameterize the redshift error as a function of redshift. The equation after residual minimization is described in Equation (5), and we adopt the output of Equation (5) evaluated at each BCG photometric redshift as the error on said redshift as summarized in Figure 3.

$$\sigma_z(z) = \sqrt{3.69 \times 10^{-5} + 9.15 \times 10^{-2} \times z^{3.40}} \Big|_{z_{\text{BCG}}} \quad (5)$$

2.3. Source Redshift

The redshift of the source does not significantly alter the final mass measurement of the data (Remolina González et al. 2020), and it only introduces a bias factor into the final measurement. The “average” population of source redshift arcs can be fitted by a Gaussian with $\mu = 2$ and $\sigma = 0.2$ (Bayliss et al. 2011), and we simply adopt this distribution for source redshifts among all strong-lensing systems in this sample.

2.4. Cluster Light

Conveniently, the pixel values in the Legacy Survey DR9 DECaLS fits images that are the backbone of the analysis in this work are in units of nanomaggies: a linear unit of flux that is normalized to the AB magnitude system where 1 nanomaggie = 3.63078×10^{-20} erg/s/cm²/Hz. Initial estimates for cluster light were generated by linearly summing the flux from all pixels in each of the *grz* filter images from DECaLS within a circular aperture centered at the BCG with radius equal to the measured Einstein radius for each system. Careful attention was paid to ensuring that this step did not include light from the lensed sources, as well as any intervening stars or foreground galaxies as identified by a flux and visual color screening. This was accomplished by creating two separate mask files: one to mask the flux from source arcs, and another to mask flux from interlopers. Both were made with a custom IDL script that allows the user to “paint” regions in an image with a circular brush and save the painted regions to a fits file. The light integration step was carried out for the 1000 different bootstrapped radii defined when the Einstein radius was fitted, and the resulting mean and standard deviation for the 1000 light measurements after correcting each for Milky Way extinction in each filter at the location of the BCG were adopted as the characteristic value and error respectively for all 179 clusters in the sample. While this technique does not necessarily account for every possible source of systematic uncertainty (mis-identification of cluster members, accidental masking of intracluster light, etc.), any slight source of uncertainty in these measurements is likely outweighed from uncertainty in our bootstrapping step or in the uncertainty in the photometric fitting algorithm we describe in Section 3.

3. ANALYSIS

3.1. Light Measurements

In order to robustly constrain stellar mass and light, the measured flux density in nanomaggies for all the photometric *grz* filters in each of our strong lensing systems were fed to the parametric SED modeling pack-

age `astro-prospector` (Johnson et al. 2021), henceforth referred to as "Prospector", as initial constraints. Prospector combines the stellar population synthesis library `python-FSPS` (Flexible Stellar Population Synthesis, Conroy et al. 2009; Conroy & Gunn 2010) along with the modern MCMC model optimization package `emcee` (Foreman-Mackey et al. 2013) to interpolate a physically-motivated spectral energy distribution (SED) based on either observed photometry or observed spectroscopic data. In our case, the parametric SED for each system was fitted based on the *grz* photometry with three fixed parameters and five free parameters. Namely, we assume a Chabrier IMF (Chabrier 2003), Calzetti attenuation curve for dust (Calzetti et al. 2000), and delayed-tau SFH model (Carnall et al. 2019). We fit for stellar mass with a log-uniform prior ranging from 10^8 to $10^{14} M_{\odot}$, the log of solar metallicity with a tophat prior ranging from -1.0 to 0.2 dex, the dust attenuation coefficient used by the Calzetti dust attenuation curve with a tophat prior ranging from 0 to 2.0, the age of the cluster with a tophat prior ranging from the age of the universe at $z = 20$ to the age of the universe at the redshift of the lensing cluster in Gyr, and the value for tau in the delayed-tau SFH model with a log-uniform prior ranging from 0.1 to 10 Gyr. We utilize `emcee` as implemented in Prospector with 84 walkers for a total of 6720 iterations, taking only the last 840 iterations for each of the 84 walkers (70,560 total parameter vectors) as representing the prior distribution for each of the variables of interest in order to eliminate the significant burn-in sequence of the fit. After fitting, we adopt the 50th percentile value as the characteristic value for each of the five parameters, and the greater difference between the 84th-50th percentile and 50th-16th percentile values as the error for each of the five parameters. An example of a resulting spectrum from this fitting process is shown in Figure 4.

To generate light estimates, we take a random sample of 1024 parameter vectors for mass, dust, metallicity, age, and tau drawn from the posterior distribution of 70,540 returned by Prospector and generate an SED for each based on these parameters. We then integrate over the rest-frame wavelength range of $3000\text{\AA} - 7000\text{\AA}$ shifted into the observed frame according to the BCG redshift for each of the sample SEDs to convert to an observed flux in erg/s/cm^2 as summarized in Equation (6).

$$\text{Flux} \left[\frac{\text{erg}}{\text{cm}^2 \text{s}} \right] = \int_{3000\text{\AA} \times (1+z)}^{7000\text{\AA} \times (1+z)} I(\lambda) d\lambda \quad (6)$$

The wavelength range covered by the *g*-band, *r*-band, and *z*-band filters spans from $\approx 4000\text{\AA}$ to $10,000\text{\AA}$, so a range of $3000\text{\AA} - 7000\text{\AA}$ allows us to sample impor-

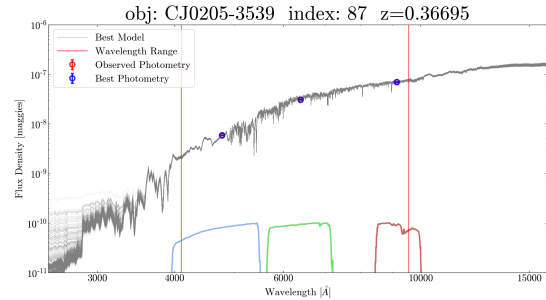


Figure 4. A spectral energy distribution for CJ0205-3539, one of the 179 clusters in our sample, after running a Prospector analysis. SEDs for 1000 random parameter vectors drawn from the final chain of 70,560 are plotted in grey. The blue, green, and red curves represent the transmission curves (in arbitrary units) for the *g*-band, *r*-band, and *z*-band filters as a function of wavelength respectively. The left and right vertical red lines mark 3000\AA and 7000\AA respectively redshifted by the redshift of the cluster. We integrate for luminosity between them.

tant features in the restframe optical such as the 4000\AA break, while also remaining physically motivated by flux in the *z*-band as the lower bound of 3000\AA gets redshifted out of the *g* and *r* bands in the observed frame. As can be seen in Figure 4, the scatter between the sample SEDs grows outside the rest-frame wavelength coverage range of the *grz* filters, and so staying as close to them as possible while still measuring over a reasonable wavelength range is desirable. After integrating our SED to obtain flux, we convert the observed flux to a luminosity in solar luminosities using Equations (7) and (8) where $d_L(z_{\text{BCG}})$ is the luminosity distance at the redshift of the BCG.

$$L [\text{erg}] = (\text{Eq. 6}) \times 4\pi[d_L(z_{\text{BCG}})]^2 \quad (7)$$

$$L [L_{\odot}] = (\text{Eq. 7}) \times \left(3.846 \times 10^{33} \left[\frac{\text{erg}}{\text{s}} \right] \right)^{-1} \quad (8)$$

After luminosity calculations were carried out for our 1024 randomly sampled SEDs, we once again adopt the 50th percentile value as the characteristic value for luminosity, and the greater difference between the 84th-50th percentile and 50th-16th percentile values as the error for luminosity in each of the galaxy clusters.

3.2. Stellar Mass Measurements

Estimates for stellar mass in each system were also generated as a result of the Prospector fitting. Since stellar mass is one of the parameters used by Prospector to parameterize an SED, we can infer the stellar mass for each system from the posterior distribution of each fit. An example of such posterior is shown in Figure 5.

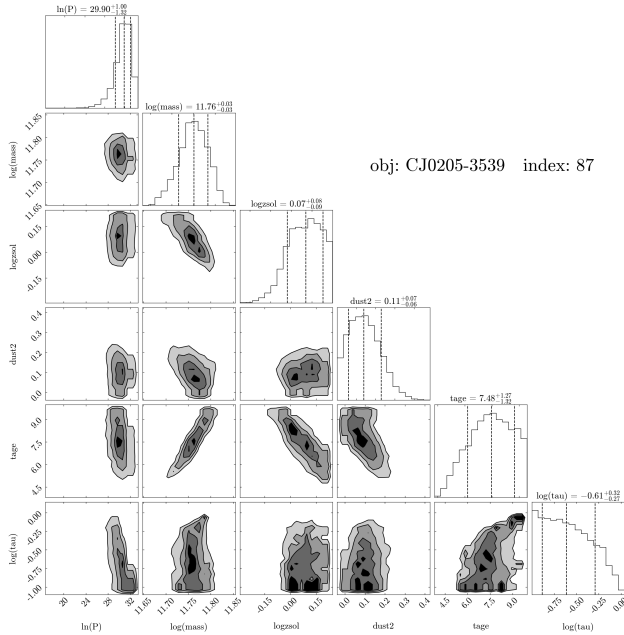


Figure 5. A corner plot of the fitted parameters describing the SED for CJ0205-3539, one of the 179 clusters in our sample, after running a Prospector analysis.

However, the stellar mass reported by Prospector describes the total stellar mass formed over the lifetime of the galaxy. Since stars in galaxies are subject to dynamical events such as supernovae, mergers, and outflows (e.g., Li et al. 2017), the stellar mass that constitutes the light we see at observation is not necessarily all the stellar mass that has formed in the history of that galaxy. What we are actually interested in is the amount of stellar mass that we currently see at the time of observation. Prospector parameterizes this value in the form of a surviving mass fraction that is generated once a fit is complete. We obtain the observed stellar mass at the time of observation by multiplying the 50th percentile value for the stellar mass posterior by the surviving mass fraction. The greater difference between the 84th-50th percentile and 50th-16th percentile values was adopted as the error for stellar mass in each of the galaxy clusters.

3.3. Total Mass Measurements

Once measurements for the Einstein radius, source redshift, and lens redshift were robustly measured, we calculated the enclosed cluster mass using Equations (3) and (4) via Monte Carlo statistical methods. The enclosed cluster mass was computed 1000 times, and each calculation used a different Einstein radius, source redshift, and lens redshift randomly drawn from a Gaussian prior with standard deviation equal to the uncertainty on each measurement and mean equal to the charac-

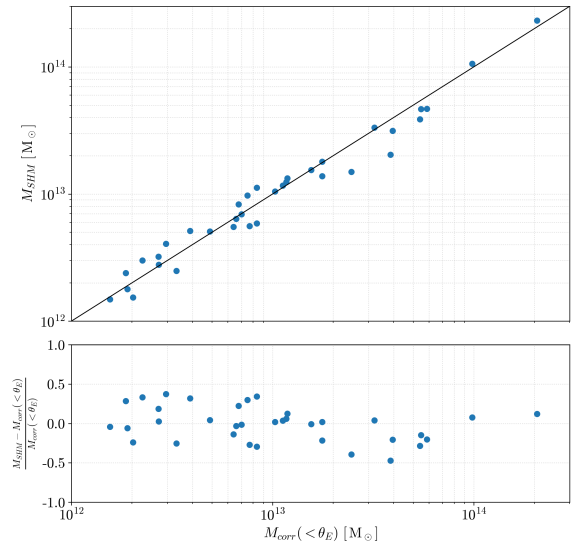


Figure 6. A comparison between mass estimates generated by the LENSTOOL analysis plotted on the y-axis, and mass estimates generated by evaluating Equations (3), (4), and (9) plotted on the x-axis for the first 35 clusters analyzed in our sample. A fractional difference plot between the two is shown below. Note the similar scatter between the two measurements over a wide range of mass scales.

teristic value for each measurement. Also described in Remolina González et al. (2020) is the need to apply an empirical correction based on the “completeness” of the lensed galaxy arcs in each system of the following form:

$$\text{Corrected } M(< \theta_E) = \frac{\text{Measured } M(< \theta_E)}{f(\theta_E)} \quad (9)$$

Where $f(\theta_E)$ is a parabolic function specified in Remolina González et al. (2020).

For the purposes of applying this correction in each of our 179 clusters, we define the azimuthal coverage as the percentage of a full Einstein ring traced out by the lensed galaxy arcs in a given system. For example, a lens with a tangential arc stretching from 3 o’clock to 6 o’clock (where North is 12 o’clock) would have an azimuthal coverage of 0.25. This was measured by determining what fraction of a circle with the best-fit Einstein radius centered at the BCG fell within the painted region representing the lensed source arcs. If the measured azimuthal coverage was less than 0.5, Equation (9) was applied. If greater than or equal to 0.5, it was not applied. The mean and standard deviation of the resulting 1000 measurements after accounting for the empirical correction were adopted as its characteristic mass and

error. In constraining mass, we also considered a second method for measuring the cluster-centric mass elucidated in Remolina González et al. (2021a) that leverages the parametric lens modeling software LENSTOOL (Jullo et al. 2007) to estimate the enclosed mass as opposed to the simple evaluation of Equations (3), (4), and (9). For the first 35 clusters that were analyzed as a part of this work, we generated single-halo lens models using LENSTOOL by using the three coordinates corresponding to the locations of the brightest clumps in each lensed arc as positional constraints with a single pseudo-isothermal elliptical mass distribution (PIEMD, Kassiola & Kovner 1993) locked to the center of the BCG. The software then runs an MCMC sampler to constrain the best-fit halo that recreates the observed positions of the position constraints for the main multiple image family. A fits file for each system where the pixel values correspond to $10^6 M_{\odot}$ contained in that pixel was outputted by LENSTOOL to describe the best-fit mass distribution found by the MCMC sampling. We then linearly integrated this mass sheet over a circular aperture centered on the coordinates of the BCG with area equal to the area enclosed by the tangential critical curve as prescribed in Remolina González et al. (2021a). The primary downside to this method is speed, and it is also sensitive to the choice of defining locations along the lensed arc in a way that simple circle fitting is not. While it is possible to refine the positional constraints based on the output of each lens model, the process of iteratively refining just one lens model for a single system may take upwards of an hour for a single system, whereas evaluating Equations (3), (4), and (9) takes only moments. In addition, the positional constraints that are ultimately fed to these equations in the process of measuring the Einstein radius need not be extremely accurate with respect to exactly constraining image family positions since, as long as the positional constraints are accurately placed at any point along the tangentially lensed images, the method is accurate to within the systematic uncertainty. A comparison of these two estimates in Figure 6 shows a well-described scatter over a wide range of enclosed masses as expected from Remolina González et al. (2021b), and we use the simplest estimate from Equations (3), (4), and (9) hereafter.

4. RESULTS

4.1. Stellar-to-Total-Mass Ratio

Now that we have measured the total mass constrained by lensing as well as stellar mass constrained by photometric analysis, we are able to take the ratio of the two to generate a stellar-to-total-mass ratio measurement. At the onset of this work, one of the ques-

tions we grappled with was whether or not there was any difference in the stellar-to-total-mass ratio as a function of the three different types of strong lensing, as well as whether there were different trends for just BCG light, or cluster members at large. Before plotting, each image in the sample was visually classified with two labels. The first label simply marked whether or not the Einstein radius enclosed only one galaxy or multiple galaxies. The second label was a visual ranking of the perceived richness of each system which labeled systems as either galaxy-scale, group-scale, or cluster-scale lensing. When plotting Einstein radius against the stellar-to-total-mass ratio, we used these labels to plot each cluster with a unique marker to see if there were any immediately visible trends.

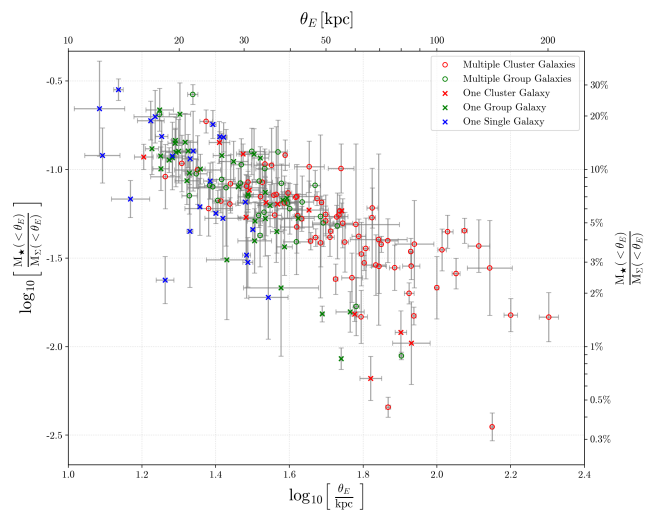


Figure 7. The Einstein radius converted to a physical kiloparsec distance based on the angular diameter distance at the redshift of the BCG plotted against the stellar-to-total-mass ratio. Points are color-coded and styled according to a visual classification that separated them by visible richness and whether or not the Einstein radius enclosed more than just the BCG for each system.

We note that there is a gradient (as expected) to Figure 7 insofar as clusters of galaxies are heavily concentrated on the right hand side of Figure 7, whereas group-scale and relatively isolated galaxies are more concentrated on the left side of the Figure 7. Figure 8 presents the same data, now color-coded by the total enclosed stellar luminosity, to further illuminate this trend.

As visible in both Figure 7 and Figure 8, there is a clearly negative correlation between these two parameters. Also shown in Figure 8 are 500 random samples drawn from the posterior distribution of a linear regression also done with the MCMC package `emcee`. We include an intrinsic Gaussian scatter on the y-axis to

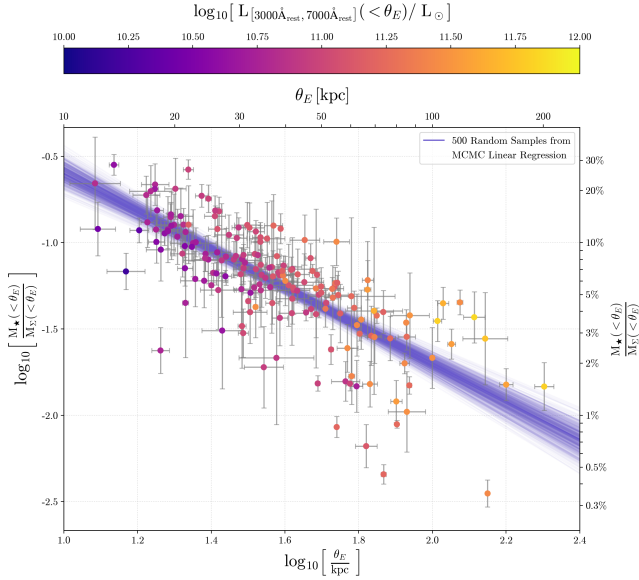


Figure 8. The Einstein radius converted to a physical kiloparsec distance based on the angular diameter distance at the redshift of the BCG plotted against the stellar-to-total-mass ratio. The points are color-coded according to the luminosity of the system in units of solar luminosities from stellar light within the aperture defined by the Einstein radius as measured in the rest-frame wavelength range from 3000Å to 7000Å.

this model in order to describe the luminosity differences in each system that account for much of the scatter in the plot. The results of the fit and their corresponding $\pm 1\sigma$ uncertainties are shown in Table 1.

Table 1. Linear Fit Parameters

m	b	σ_y
$-1.10^{+0.08}_{-0.08}$	$0.50^{+0.12}_{-0.12}$	$0.2^{+0.01}_{-0.01}$

4.2. Total-Mass-to-Light Ratio

One of the chief goals of this work is to robustly measure the total-mass-to-light ratio of a sample of galaxy cluster cores over a wide range of redshifts leveraging the effects of strong gravitational lensing to place tight constraints on the total mass of the cluster at smaller angular scales than other methods would allow. Again leveraging the total mass constrained by lensing as well as stellar light constrained by photometric analysis, we are able to take the ratio of the two to generate a total-mass-to-light ratio measurement. We apply standard

error propagation techniques for the error on the M/L ratio as well. Figure 9 shows the resulting total-mass-to-light ratio as a function of redshift for the entire sample.

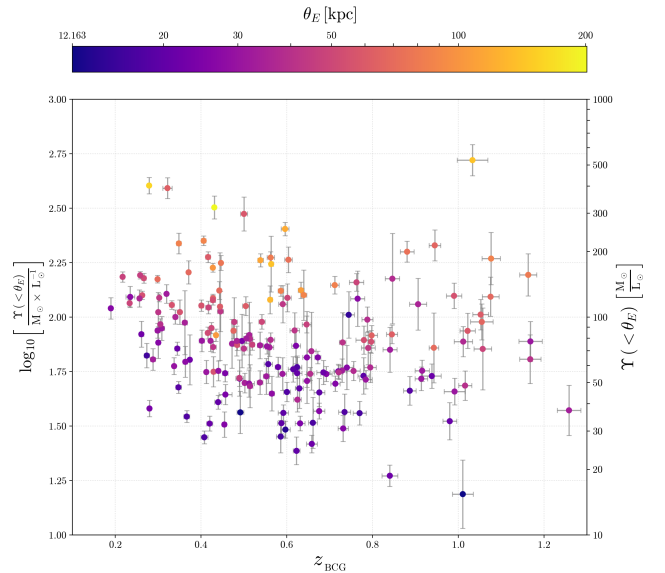


Figure 9. The photometric redshift of the BCG plotted against the total-mass-to-light ratio. The points are colored according to the Einstein radius converted to a physical kiloparsec distance based on the angular diameter distance at the redshift of the BCG.

There is also little correlation between the mass-to-light ratio and BCG redshift. While the Pearson correlation coefficient is -0.167 , which for our sample of 179 clusters would lead to a p-value of 0.025 (a marginally significant result), we believe this is primarily a function of the selection effect of our survey. The bottom left of Figure 9 would be populated with low Einstein radius clusters at a low redshift, but since this Einstein radius scale is on order of about 10 kiloparsecs, any Einstein rings visible would be visually located right on top of the BCG light. This would not only make them hard to detect based on the COOL-LAMPS visual search algorithm, but it would also make them unsuitable for this analysis because the source light would be completely blended together with the lensing cluster light. The top right of Figure 9 would be primarily populated by clusters at a high redshift with large Einstein radii, which are simply a rarer type of lensing system in the universe (Collett 2015). Since this work uses the effects of gravitational lensing to measure the total-mass-to-light ratio in the first place, we are systematically biased against finding and plotting such systems in Figure 9. Since the COOL-LAMPS visual search algorithm is primarily based on DECaLS DR8 images, many of these high-redshift clusters barely even show up in the z-band filter

images. We may simply not have scanned enough of the sky to find many examples of these systems. Therefore, we posit that this work is unable to show any statistically significant evolution of the total-mass-to-light ratio as a function of redshift as informed by measuring this value directly across a wide range of redshifts and physical distance scales.

5. CONCLUSION

We have shown that an algorithmic measurement of mass and light in many different types of strong lensing

systems is possible. Leveraging a wide variety of computational techniques, we have shown that there is a negative correlation between the distance from the BCG and the stellar-to-total-mass ratio and have robustly parameterized it. We have also shown little correlation between the total-mass-to-light ratio as a function of redshift, and have discussed possible systematic biases for these measurements. Further study will be done to compare these measurements to the literature, and follow-up work/observations will be done in order to tighten our statistical/systematic uncertainties.

REFERENCES

- Bayliss, M. B., Gladders, M. D., Oguri, M., et al. 2011, *ApJL*, 727, L26, doi: [10.1088/2041-8205/727/1/L26](https://doi.org/10.1088/2041-8205/727/1/L26)
- Bryan, G. L., & Norman, M. L. 1998, *ApJ*, 495, 80, doi: [10.1086/305262](https://doi.org/10.1086/305262)
- Calzetti, D., Armus, L., Bohlin, R. C., et al. 2000, *ApJ*, 533, 682, doi: [10.1086/308692](https://doi.org/10.1086/308692)
- Carnall, A. C., Leja, J., Johnson, B. D., et al. 2019, *ApJ*, 873, 44, doi: [10.3847/1538-4357/ab04a2](https://doi.org/10.3847/1538-4357/ab04a2)
- Chabrier, G. 2003, *PASP*, 115, 763, doi: [10.1086/376392](https://doi.org/10.1086/376392)
- Collett, T. E. 2015, *ApJ*, 811, 20, doi: [10.1088/0004-637X/811/1/20](https://doi.org/10.1088/0004-637X/811/1/20)
- Conroy, C., & Gunn, J. E. 2010, *ApJ*, 712, 833, doi: [10.1088/0004-637X/712/2/833](https://doi.org/10.1088/0004-637X/712/2/833)
- Conroy, C., Gunn, J. E., & White, M. 2009, *ApJ*, 699, 486, doi: [10.1088/0004-637X/699/1/486](https://doi.org/10.1088/0004-637X/699/1/486)
- Dey, A., Schlegel, D. J., Lang, D., et al. 2019, *AJ*, 157, 168, doi: [10.3847/1538-3881/ab089d](https://doi.org/10.3847/1538-3881/ab089d)
- Einstein, A. 1936, *Science*, 84, 506, doi: [10.1126/science.84.2188.506](https://doi.org/10.1126/science.84.2188.506)
- Foreman-Mackey, D., Hogg, D. W., Lang, D., & Goodman, J. 2013, *PASP*, 125, 306, doi: [10.1086/670067](https://doi.org/10.1086/670067)
- Forman, W., Kellogg, E., Gursky, H., Tananbaum, H., & Giacconi, R. 1972, *ApJ*, 178, 309, doi: [10.1086/151791](https://doi.org/10.1086/151791)
- Gladders, M. D., & Yee, H. K. C. 2000, *AJ*, 120, 2148, doi: [10.1086/301557](https://doi.org/10.1086/301557)
- Gunn, J. E., Kristian, J., Oke, J. B., Westphal, J. A., & Young, P. J. 1979, *IAUC*, 3431, 2
- Honscheid, K., & DePoy, D. L. 2008, arXiv e-prints, arXiv:0810.3600, doi: [10.48550/arXiv.0810.3600](https://doi.org/10.48550/arXiv.0810.3600)
- Hradecky, V., Jones, C., Donnelly, R. H., et al. 2000, *ApJ*, 543, 521, doi: [10.1086/317158](https://doi.org/10.1086/317158)
- Johnson, B. D., Leja, J., Conroy, C., & Speagle, J. S. 2021, *ApJS*, 254, 22, doi: [10.3847/1538-4365/abef67](https://doi.org/10.3847/1538-4365/abef67)
- Jullo, E., Kneib, J. P., Limousin, M., et al. 2007, *New Journal of Physics*, 9, 447, doi: [10.1088/1367-2630/9/12/447](https://doi.org/10.1088/1367-2630/9/12/447)
- Kassiola, A., & Kovner, I. 1993, *ApJ*, 417, 450, doi: [10.1086/173325](https://doi.org/10.1086/173325)
- Kellogg, E., Gursky, H., Tananbaum, H., Giacconi, R., & Pounds, K. 1972, *ApJL*, 174, L65, doi: [10.1086/180950](https://doi.org/10.1086/180950)
- Kuiper, G. P. 1938, *ApJ*, 88, 472, doi: [10.1086/143999](https://doi.org/10.1086/143999)
- Levine, B. 2022, doi: <https://doi.org/10.6082/uchicago.4947>
- Li, M., Bryan, G. L., & Ostriker, J. P. 2017, *ApJ*, 841, 101, doi: [10.3847/1538-4357/aa7263](https://doi.org/10.3847/1538-4357/aa7263)
- Lotz, J. M., Koekemoer, A., Coe, D., et al. 2017, *ApJ*, 837, 97, doi: [10.3847/1538-4357/837/1/97](https://doi.org/10.3847/1538-4357/837/1/97)
- Lourenço, A. C. C., Lopes, P. A. A., Laganá, T. F., et al. 2020, *MNRAS*, 498, 835, doi: [10.1093/mnras/staa2464](https://doi.org/10.1093/mnras/staa2464)
- Markevitch, M., & Vikhlinin, A. 2007, *PhR*, 443, 1, doi: [10.1016/j.physrep.2007.01.001](https://doi.org/10.1016/j.physrep.2007.01.001)
- Napier, K., Gladders, M., Sharon, K., et al. 2023, arXiv e-prints, arXiv:2305.14317, doi: [10.48550/arXiv.2305.14317](https://doi.org/10.48550/arXiv.2305.14317)
- Navarro, J. F., Frenk, C. S., & White, S. D. M. 1996, *ApJ*, 462, 563, doi: [10.1086/177173](https://doi.org/10.1086/177173)
- Presotto, V., Girardi, M., Nonino, M., et al. 2014, *A&A*, 565, A126, doi: [10.1051/0004-6361/201323251](https://doi.org/10.1051/0004-6361/201323251)
- Remolina González, J. D., Sharon, K., Li, N., et al. 2021a, *ApJ*, 910, 146, doi: [10.3847/1538-4357/abe62a](https://doi.org/10.3847/1538-4357/abe62a)
- Remolina González, J. D., Sharon, K., Reed, B., et al. 2020, *ApJ*, 902, 44, doi: [10.3847/1538-4357/abb2a1](https://doi.org/10.3847/1538-4357/abb2a1)
- Remolina González, J. D., Sharon, K., Mahler, G., et al. 2021b, *ApJ*, 920, 98, doi: [10.3847/1538-4357/ac16d8](https://doi.org/10.3847/1538-4357/ac16d8)
- Rivera-Thorsen, T. E., Dahle, H., Gronke, M., et al. 2017, *A&A*, 608, L4, doi: [10.1051/0004-6361/201732173](https://doi.org/10.1051/0004-6361/201732173)
- Rubin, V. C. 1986, *Highlights of Astronomy*, 7, 27
- Shajib, A. J., Vernardos, G., Collett, T. E., et al. 2022, arXiv e-prints, arXiv:2210.10790, doi: [10.48550/arXiv.2210.10790](https://doi.org/10.48550/arXiv.2210.10790)
- Wang, J., & Zhong, Z. 2018, *A&A*, 619, L1, doi: [10.1051/0004-6361/201834109](https://doi.org/10.1051/0004-6361/201834109)

White, M. 2001, *A&A*, 367, 27,

doi: [10.1051/0004-6361:20000357](https://doi.org/10.1051/0004-6361:20000357)

Zwicky, F. 1933, *Helvetica Physica Acta*, 6, 110